

A surface-aware projection basis for quasigeostrophic flow

K. SHAFER SMITH*

*Center for Atmosphere Ocean Science
Courant Institute of Mathematical Sciences
New York University
New York, NY*

JACQUES VANNESTE

*School of Mathematics
University of Edinburgh
Edinburgh, United Kingdom*

Submitted to JPO

8 March 2013

**Corresponding author address:* K. Shafer Smith, Courant Institute of Mathematical Sciences,
New York University, 251 Mercer St., New York, NY 10012.

E-mail: shafer@cims.nyu.edu

ABSTRACT

Recent studies indicate that altimetric observations of the ocean's mesoscale eddy field reflect the combined influence of surface buoyancy and interior potential vorticity anomalies. The former have a surface-trapped structure, while the latter have a more grave form. To assess the relative importance of each contribution to the signal, it is useful to project the observed field onto a set of modes that separates their influence in a natural way. However, the surface-trapped dynamics are not well-represented by standard baroclinic modes; moreover, they are dependent on horizontal scale.

Here we derive a modal decomposition that results from the simultaneous diagonalization of the energy and a generalization of potential enstrophy that includes contributions from the surface buoyancy fields. This approach yields a family of orthonormal bases that depend on two parameters: the standard baroclinic modes are recovered in a limiting case, while other choices provide modes that represent surface and interior dynamics in an efficient way.

For constant stratification, these modes consist of symmetric and antisymmetric exponential modes that capture the surface dynamics, and a series of oscillating modes that represent the interior dynamics. Motivated by the ocean, where shears are concentrated near the upper surface, we also consider the special case of a quiescent lower surface. In this case, the interior modes are independent of wavenumber, and there is a single exponential surface mode that replaces the barotropic mode. We demonstrate the use and effectiveness of these modes by projecting the energy in a set of simulations of baroclinic turbulence.

1. Introduction

Because direct observations of the ocean's interior are sparse, satellite altimetry plays a crucial role in determining its time-dependent, three-dimensional velocity structure. This indirect measurement process assumes that sea surface height variations are dominated by currents with low-mode vertical structure, a result of the stiffening action of rotation and ensuing barotropization. Observations provide some support for this assumption, at least on lateral scales of order the first internal deformation scale and above. For example, using currentmeter records in conjunction with satellite observations, Wunsch (1997) argues that the bulk of the ocean's eddy kinetic energy resides in the barotropic and first baroclinic modes. In addition, a number of studies show a strong correlation between the lateral size of eddies and the first internal deformation scale (e.g. Stammer 1997; Chelton et al. 2011).

However, recent theoretical developments, supported by simulation and improved analysis of satellite altimetry, suggest that surface signals are not well-correlated with low-mode vertical structure, especially for submesoscale motions. In particular, Lapeyre and Klein (2006) argue that surface buoyancy and upper-ocean potential vorticity are anti-correlated for eddying flow, and that the three-dimensional velocity field may be obtained, assuming quasigeostrophy, from knowledge of the surface buoyancy field alone. The dynamics at the upper surface in this view are closely related to the surface quasigeostrophic (SQG) model (Blumen 1982; Held et al. 1995), and imply a vertical structure with a surface-trapped component that is not well represented by standard baroclinic modes. This view is supported by results from simulations (LaCasce and Mahadevan 2006; Klein et al. 2008), as well as recent analyses of satellite altimetry (e.g. Isern-Fontanet et al. 2006; Le Traon et al. 2008). Finally, in an atmospheric context, Tulloch and Smith (2009) have shown that lateral surface buoyancy gradients may interact with interior mean potential vorticity gradients to excite baroclinically unstable modes that generate SQG-like dynamics near the upper surface. In simulations, the resulting kinetic energy spectrum near the surface exhibits a steep -3 slope just below the deformation scale, and a flatter $-5/3$ slope at smaller scales — translated to

the oceanic context, this implies an energetic submesoscale dominated by the surface mode.

One of the most widely used tools in oceanography is the projection of the vertical structure of observed or simulated currents on simple bases of functions. The above observations and modeling results lead one to seek projection bases that faithfully represent both the low-mode interior structure and the surface dynamics. The standard basis of baroclinic modes, consisting of the eigenfunctions $\phi(z)$ of the operator $\partial_z[f^2/N^2(z) \partial_z\phi]$, with homogenous boundary conditions $\partial_z\phi|_{z=0} = \partial_z\phi|_{z=-H} = 0$, fails in this respect. By construction, it is a complete basis in which to expand the streamfunction ψ of flows provided they satisfy the same homogeneous boundary conditions, which imply zero surface and bottom buoyancy. But for realistic flows with non-zero surface buoyancy $b = f\partial_z\psi|_{z=0}$, expansion in baroclinic modes leads to a non-uniform convergence near $z = 0$, and a very large set of modes is required to capture the near-surface behaviour.

As noted by Lapeyre and Klein (2006), in quasigeostrophic theory, the dynamical contribution of the surface buoyancy can be separated from that of the interior potential vorticity: taking advantage of the linearity of the inversion of the quasigeostrophic potential vorticity (PV)

$$q = \nabla^2\psi + \partial_z \left(\frac{f^2}{N^2} \partial_z\psi \right) \quad (1)$$

the streamfunction may be decomposed into interior and surface parts, $\psi = \psi^{\text{int}} + \psi^{\text{surf}}$ (assuming zero buoyancy at the bottom), where ψ^{int} satisfies (1) with boundary condition $\partial_z\psi^{\text{int}}|_{z=0} = 0$ while ψ^{surf} satisfies the zero-PV condition $\nabla^2\psi^{\text{surf}} + \partial_z(f^2/N^2 \partial_z\psi^{\text{surf}}) = 0$ with $\partial_z\psi^{\text{surf}}|_{z=0} = b/f$. The vertical structure of the interior contribution can be expanded in the standard baroclinic modes. By contrast, the surface contribution — the only one retained in SQG theory — has a vertical structure determined by the zero PV condition which couples horizontal and vertical dependence, reducing to $\exp(\kappa Nz/f)$, where κ is the horizontal wavenumber, in the case of constant N and for $z \gg H$.

It is intuitively clear that an effective projection basis should somehow combine modes similar to the baroclinic modes with modes that, like the exponential modes of SQG theory,

capture the dynamical contribution of the surface buoyancy. A systematic method to obtain such a basis has remained elusive, however. Tulloch and Smith (2009) proposed a heuristic model based on a barotropic and first baroclinic mode, appended by exponential modes for each surface. Similarly, Lapeyre (2009) attempted to represent the full dynamics of the upper ocean with a truncated set of standard baroclinic modes appended by an exponential surface mode. However, these hybrid modes do not diagonalize the energy, since the surface and interior modes are not orthogonal. Moreover, because the surface modes depend on wavenumber while the interior modes do not, the energetic overlap varies with horizontal scale, increasing with increasing scale. These difficulties stem from the fact that the addition of the exponential mode makes the basis functions linearly dependent in a certain sense, leading to an overcomplete frame rather than a basis. A consequence is that the modal decomposition is non-unique. Lapeyre (2009) defined a unique basis by requiring that it minimizes a certain functional, but the results remained inconclusive. An alternative basis, involving modes satisfying the Dirichlet condition $\psi|_{z=0} = 0$ together with the barotropic mode, has recently been proposed by Scott and Furnival (2012) but this too suffers from a lack of orthogonality.

In this paper, we take a different approach and propose a new modal basis (or rather a family of bases) that diagonalizes the energy and effectively captures surface-intensified motion driven by buoyancy. Our approach relies on the observation that there are infinitely many possible (complete) bases onto which the flow may be projected which diagonalize the energy. As we show, a useful basis is obtained by demanding that it simultaneously diagonalizes both the energy and another quadratic invariant that generalizes potential enstrophy to include the variances of the surface and bottom buoyancy fields. The relative weight of the potential enstrophy and buoyancy variances in this invariant provide two parameters that determine the basis uniquely.

The eigenvalue problem that arises is similar to the standard vertical mode problem, but retains a dependence on horizontal wavenumber, and the eigenvalue appears in both the

114 eigenvalue equation and its boundary conditions. In a limiting case, the standard baroclinic
 115 modes are recovered — for constant N and $-H \leq z \leq 0$, these are $\psi_n \propto \cos(n\pi z/H)$, $n =$
 116 $0, 1, \dots$. Another limiting case, motivated by the ocean where shears are concentrated near
 117 the upper surface but are weak at depth, leads to the simple basis

$$\psi_0 \propto \cosh [N\kappa(z + H)/f], \quad \psi_n \propto \sin [(n - 1/2)\pi z/H], \quad n = 1, 2, \dots \quad (2)$$

118 which includes the exponential mode of SQG theory.

119 The paper is organized as follows. In section 2 we construct a generalized eigenvalue
 120 problem that defines the new basis. In section 3, we derive analytical solutions and general
 121 results for two special cases: constant N , for expository purposes, and an ocean-like case,
 122 in which the lower boundary is assumed quiescent, leading to (2). These modes are tested
 123 in section 4 on fields generated from a set of high-resolution quasigeostrophic simulations of
 124 baroclinic turbulence. Finally, we discuss and conclude in section 5.

125 2. Surface-aware basis

Throughout the paper, we assume a horizontally-periodic domain bounded vertically by rigid surfaces at $z = z^-$ and $z = z^+$, with total depth $H = z^+ - z^-$. The horizontal periodicity allows us to Fourier transform the equations in the horizontal plane, resulting in separable dynamics and ordinary differential equations for the vertical structure. (In more general domains, the Fourier series can be replaced by an expansion in eigenfunctions of the horizontal Laplacian, and the results obtained here should hold essentially unchanged.) The complex amplitudes of the quasigeostrophic potential vorticity (PV) $q = q_{kl}(z)$, surface buoyancies (SBs) b_{kl}^\pm and streamfunction $\psi = \psi_{kl}(z)$ are then related by

$$\left(\frac{f^2}{N^2} \psi' \right)' - \kappa^2 \psi = q, \quad z^- < z < z^+ \quad (3a)$$

$$\frac{f^2}{N^2 H} \psi' = b^\pm, \quad z = z^\pm, \quad (3b)$$

126 where $\kappa = (k^2 + l^2)^{1/2}$ is the wavenumber magnitude, a prime indicates a z derivative, f
127 is the Coriolis frequency and $N = N(z)$ is the buoyancy frequency. We include the non-
128 standard factor $f^2/(N^2H)$ in our the definition of the SBs so that the SBs and PV have the
129 same dimension (inverse time), and because it ultimately yields a more natural eigenvalue
130 problem. We have omitted the wavenumber subscript on q , b^\pm and ψ and continue to do so
131 onward, except where confusion may occur.

The quasigeostrophic equation set has four quadratic invariants: energy, potential en-
strophy, and the buoyancy variance at each surface. At each wavenumber κ , these are

$$\begin{aligned} E_\kappa &= \frac{1}{2H} \int_{z^-}^{z^+} \left(\frac{f^2}{N^2} |\psi'|^2 + \kappa^2 |\psi|^2 \right) dz \\ Z_\kappa &= \frac{1}{2H} \int_{z^-}^{z^+} |q|^2 dz \\ B_\kappa^\pm &= \frac{1}{2} |b^\pm|^2. \end{aligned}$$

132 Summing each quantity over (k, l) gives the total invariant.

133 We seek to define a complete basis that diagonalizes the energy. This can be done in
134 infinitely many ways. Our strategy is based on the following principles: (i) we regard the
135 energy as a functional, not of the streamfunction, but of the PV and of the SBs; (ii) we
136 exploit standard results on the simultaneous diagonalization of quadratic forms. Principle
137 (i) is grounded in the quasigeostrophic model, which makes it explicit that PV and SBs,
138 taken together, make up the set of dynamical variables. Thus, the contribution of the SBs
139 to the dynamics is recognized; as a result, the bases we obtain naturally represent data with
140 non-zero surface buoyancies. Regarding (ii), we recall a classical result from linear algebra:
141 whereas there are infinitely many bases diagonalizing a quadratic form $\mathbf{x}^T \mathbf{A} \mathbf{x}$, where \mathbf{A}
142 is a symmetric positive definite matrix, only one of these bases also diagonalizes another
143 quadratic form $\mathbf{x}^T \mathbf{B} \mathbf{x}$ (e.g. Horn and Johnson 1990). This is simply found by solving the
144 generalized eigenvalue problem $\mathbf{B} \mathbf{x} = \lambda \mathbf{A} \mathbf{x}$. An analogous result applies to linear operators
145 (see, e.g. Goldstein 1980). Similarly, here we can define a unique basis by insisting that it
146 diagonalizes another quadratic form in addition to the energy E_κ . A natural choice for this

147 is a ‘generalized potential enstrophy’ that combines the remaining invariants into a single
 148 quantity,

$$P_\kappa \equiv Z_\kappa + \alpha_+ B^+ + \alpha_- B^- \quad (4)$$

149 where $\alpha_\pm > 0$ are (nondimensional) undetermined weights, the choice of which will be
 150 discussed later. This approach yields a unique basis for fixed α_\pm .

151 To proceed, we require four objects: a vector structure that combines the SBs and
 152 interior PV, an inner product that operates on this vector, and two operators (analogous to
 153 the matrices A and B above) that give the energy and generalized potential enstrophy in
 154 terms of the inner product. These are defined as follows:

155 **Vector.** We define the ‘generalized potential vorticity vector’¹

$$\mathbf{Q} \equiv \begin{pmatrix} b^+ \\ q(z) \\ b^- \end{pmatrix}. \quad (5)$$

156 **Inner product.** The specific choice of inner product is unimportant for the final results;
 157 we make what appears to be the simplest choice, namely

$$\langle \mathbf{Q}_1, \mathbf{Q}_2 \rangle = \frac{1}{H} \int_{z^-}^{z^+} \bar{q}_1 q_2 \, dz + \bar{b}_1^+ b_2^+ + \bar{b}_1^- b_2^-, \quad (6)$$

158 where the overbar denotes a complex conjugate.

159 **Operators.** With the definitions (5) and (6), it is a simple matter to find the linear operators
 160 \mathcal{E} and \mathcal{P} such that

$$E_\kappa = \frac{1}{2} \langle \mathbf{Q}, \mathcal{E} \mathbf{Q} \rangle \quad \text{and} \quad P_\kappa = \frac{1}{2} \langle \mathbf{Q}, \mathcal{P} \mathbf{Q} \rangle. \quad (7)$$

¹Notice that our \mathbf{Q} bears a resemblance to the generalized potential vorticity of Bretherton (1966), which in our notation is written

$$Q_B = \left(\frac{f^2}{N^2} \psi' \right)' - \kappa^2 \psi - \frac{f^2}{N^2} \psi' \delta(z - z^+) + \frac{f^2}{N^2} \psi' \delta(z - z^-).$$

Our notation makes it plain that the PV and SBs are independent, a point that the use of Q_B might obscure.

These are given by

$$\mathcal{E}\mathbf{Q} = \begin{pmatrix} \psi(z^+) \\ -\psi(z) \\ -\psi(z^-) \end{pmatrix} \quad \text{and} \quad \mathcal{P}\mathbf{Q} = \begin{pmatrix} \alpha_+ b^+ \\ q(z) \\ \alpha_- b^- \end{pmatrix}, \quad (8)$$

where the streamfunction ψ is the solution of (3), given q and b^\pm . The first of these expressions is obtained after an integration by parts; the second is immediate. These two operators are positive definite and self-adjoint (see Appendix 5 for details).

The basis we seek is now given by the eigenfunctions $\boldsymbol{\xi}_n$ of the generalized eigenvalue problem

$$\mathcal{P}\boldsymbol{\xi}_n = \mu_n^2 \mathcal{E}\boldsymbol{\xi}_n, \quad (9)$$

where the eigenvalues μ_n^2 are positive for all n . To obtain an explicit form for (9), we define the components of $\boldsymbol{\xi}_n = [\xi_n^+, \xi_n(z), \xi_n^-]^T$ analogous to those of \mathbf{Q} , and the scalar streamfunctions $\phi_n(z)$ such that $\mathcal{E}\boldsymbol{\xi}_n = [\phi_n(z^+), -\phi_n(z), -\phi_n(z^-)]^T$. In terms of these, the eigenvalue problem reads

$$\begin{pmatrix} \alpha_+ \xi_n^+ \\ \xi_n(z) \\ \alpha_- \xi_n^- \end{pmatrix} = \mu_n^2 \begin{pmatrix} \phi_n(z^+) \\ -\phi_n(z) \\ -\phi_n(z^-) \end{pmatrix}. \quad (10)$$

In view of (3), this implies that the ϕ_n satisfy

$$\left(\frac{f^2}{N^2} \phi_n' \right)' - \kappa^2 \phi_n = -\mu_n^2 \phi_n \quad \text{and} \quad \frac{f^2}{N^2 H} \phi_n' = \pm \frac{\mu_n^2}{\alpha_\pm} \phi_n \quad \text{at} \quad z = z^\pm. \quad (11)$$

This eigenvalue problem is a key result of the paper. Its eigenfunctions ϕ_n , which are purely real, give the form of the streamfunction corresponding to the basis eigenvectors $\boldsymbol{\xi}_n$. The three components of these eigenvectors may be derived from the ϕ_n using (10), although, as shown below, this is not necessary to project data onto the modes $\boldsymbol{\xi}_n$.

By construction, the eigenfunctions are orthogonal for the products $\langle \cdot, \mathcal{E} \cdot \rangle$ and $\langle \cdot, \mathcal{P} \cdot \rangle$.

The choice of normalization for the eigenvectors $\boldsymbol{\xi}_n$ is inessential, but it is convenient to fix

the energy of each mode to be unity, that is, to take

$$\langle \xi_m, \mathcal{E} \xi_n \rangle = \frac{1}{H} \int_{z^-}^{z^+} \left(\frac{f^2}{N^2} \phi'_m \phi'_n + \kappa^2 \phi_m \phi_n \right) dz = \delta_{mn}. \quad (12)$$

The expression in terms of ϕ_m and ϕ_n is found by using (10) and (11) to eliminate ξ_m , ξ_n and the eigenvalues, then integrating by parts, which removes boundary terms. Correspondingly,

$$\langle \xi_m, \mathcal{P} \xi_n \rangle = \frac{\mu_n^2}{H} \int_{z^-}^{z^+} \left(\frac{f^2}{N^2} \phi'_m \phi'_n + \kappa^2 \phi_m \phi_n \right) dz = \mu_n^2 \delta_{mn} \quad (13)$$

and

$$\langle \mathcal{P}^{-1} \mathcal{E} \xi_m, \mathcal{E} \xi_n \rangle = \frac{1}{H} \int_{z^-}^{z^+} \phi_m \phi_n dz + \frac{\phi_m(z^+) \phi_n(z^+)}{\alpha_+} + \frac{\phi_m(z^-) \phi_n(z^-)}{\alpha_-} = \mu_n^{-2} \delta_{mn}. \quad (14)$$

The latter relation (14) has the advantage of involving only the undifferentiated streamfunctions, while the first relation (12) is independent of the eigenvalues and α_{\pm} .

The basis of eigenfunctions can be used to expand data: given \mathbf{Q} or ψ , we can write

$$\mathbf{Q} = \sum_n a_n \xi_n \quad \text{and} \quad \psi = \sum_n a_n \phi_n, \quad (15)$$

where the a_n are amplitude coefficients that can be found using one of the orthogonality relations (12) or (13); for instance

$$a_n = \langle \xi_n, \mathcal{E} \mathbf{Q} \rangle = \frac{1}{H} \int_{z^-}^{z^+} \left(\frac{f^2}{N^2} \phi'_n \psi' + \kappa^2 \phi_n \psi \right) dz.$$

The energy and generalized potential enstrophy are then simply

$$E_{\kappa} = \frac{1}{2} \sum_n |a_n|^2 \quad \text{and} \quad P_{\kappa} = \frac{1}{2} \sum_n \mu_n^2 |a_n|^2, \quad (16)$$

respectively.

Note that, even though the eigenvalue problem (11) is not of the standard Sturm–Liouville form, because of the presence of the eigenvalue μ_n^2 in the boundary conditions, the basis of eigenvectors can be shown to be complete in the sense that it provides a representation of arbitrary vectors \mathbf{Q} that converges as the number of modes tends to ∞ . This is discussed further in Appendix 5.

Lastly, note that our choice of orthogonality conditions implies slightly unfamiliar dimensions for the eigenfunctions. Because $[q], [b^\pm] \sim [T^{-1}]$ and $[\mu] \sim [L^{-1}]$ (where T is time, L is length, and braces mean “dimensions of”), (9) implies that $[\xi] \sim [L^{-2}][\phi]$. The orthogonality condition (12) demands $[\phi] \sim [L]$ and therefore $[\xi] \sim [L^{-1}]$. In the next section, the problem will be analyzed in an appropriate nondimensional form.

3. Structure of the surface-aware modes and special cases

The approach described above provides a family of bases parameterized by the values of α_+ and α_- . In principle, different values can be chosen for different wavenumbers κ ; here, however, we restrict attention to choices of α_\pm that are independent of κ . To clarify some general properties of the new modes, we first recast the eigenvalue problem in non-dimensional form with the substitutions $z \mapsto Hz$, $\kappa \mapsto f/(N_0H)\kappa$ and $\mu \mapsto f/(N_0H)\mu$, where N_0 is a typical value of N ; thus the wavenumber and eigenvalue are scaled by the approximate deformation length, N_0H/f . The non-dimensional eigenvalue problem (11) then becomes

$$(s\phi'_n)' = -\lambda_n^2\phi_n \quad \text{and} \quad s\phi'_n = \pm \frac{\lambda_n^2 + \kappa^2}{\alpha_\pm} \phi_n \quad \text{at} \quad z = 0, -1, \quad \text{where} \quad s = \frac{N_0^2}{N^2(z)} \quad (17)$$

and we have defined an alternative eigenvalue λ_n such that

$$\mu_n^2 = \kappa^2 + \lambda_n^2. \quad (18)$$

Written in terms of λ_n , the eigenvalue equation takes the form of the standard vertical mode equation, but with more complicated boundary conditions.

Analysis of the new eigenvalue problem (17) is complicated by its dependence on three independent parameters: κ , α_+ and α_- . Moreover, for each choice of parameters, there is an infinite set of eigenvalues. Since the problem depends on the two weights α_\pm in a nearly

equivalent way, we proceed first by setting the weights equal and defining $\alpha \equiv \alpha_+ = \alpha_-$ (a case in which the weights differ will be considered in a later subsection). The nature of the eigenproblem is then largely determined by the size of the boundary condition coefficient μ_n^2/α : when $\mu_n^2/\alpha \rightarrow 0$, the boundary conditions revert to the standard case $\phi'_n = 0$ at the top and bottom, while when $\mu_n^2/\alpha \rightarrow \infty$, the boundary conditions become $\phi_n = 0$ at the top and bottom. However, more subtle possibilities arise as well, because unlike the standard vertical mode problem, λ_n may be imaginary (although μ_n is always real). When λ_n is real, the modes are oscillatory, but when it is imaginary, the modes are evanescent — these can be interpreted either as surface modes or as extensions of the barotropic mode.

This interpretation is suggested by examining the eigenvalue problem in two limiting regimes:

$\kappa^2 \ll \alpha$: modes with real λ satisfy the simplified boundary condition $(s\phi'_n) = \pm \lambda_n^2 \phi_n / \alpha$ at $z = 0, -1$ which further reduces to $\phi'_n = 0$ for $\alpha \gg 1$, corresponding to the standard baroclinic modes.² These are complemented by a barotropic mode for which the first approximation $\lambda = 0$ can be refined to the purely imaginary $\lambda = i\kappa\sqrt{2/\alpha}$.

$\kappa^2 \gg \alpha$. In this case, almost all modes have $\mu_n^2 = \kappa^2 + \lambda_n^2 \gg \alpha$ and hence satisfy the simplified boundary conditions $\phi_n = 0$ at $z = 0, -1$. There are two additional modes, however, for which $\mu_n^2 = O(\alpha)$ and hence $\lambda \sim i\kappa$. These solve

$$(s\phi'_n)' - \kappa^2 \phi_n \simeq 0 \quad \text{with} \quad s\phi'_n = \pm \frac{\mu_n^2}{\alpha_{\pm}} \phi_n \quad \text{at} \quad z = 0, -1, \quad (19)$$

and can be recognized as surface modes, with zero interior PV.

²This approximation is not uniform in n but breaks down for highly oscillatory modes, with $\lambda_n = O(\alpha)$, which satisfy $\phi' = O(\alpha) \neq 0$ at $z = 0, -1$ and thus differ from the standard high- n baroclinic modes.

235 *a. Analytical solutions for constant N*

236 In the special case of constant stratification, or $s = 1$, the eigenvalue problem (17) can
 237 be solved in closed form. Writing the solutions as

$$\phi_n = A \cos(\lambda_n z) + B \sin(\lambda_n z),$$

238 where A and B are integration constants, and imposing the boundary conditions leads to
 239 an algebraic equation for λ_n , which may be either real or imaginary. For $\lambda_n^2 > 0$, the
 240 characteristic equation (dropping the subscript n) is

$$\tan \lambda = \frac{(\alpha_+ + \alpha_-)\lambda(\lambda^2 + \kappa^2)}{(\lambda^2 + \kappa^2)^2 - \alpha_+ \alpha_- \lambda^2}. \quad (20)$$

241 For $\lambda^2 < 0$ we define $\tilde{\lambda} = i\lambda$ and obtain

$$\tanh \tilde{\lambda} = \frac{(\alpha_+ + \alpha_-)\tilde{\lambda}(\kappa^2 - \tilde{\lambda}^2)}{(\kappa^2 - \tilde{\lambda}^2)^2 + \alpha_+ \alpha_- \tilde{\lambda}^2}. \quad (21)$$

242 Equations (20) and (21) are suitable for a graphical analysis. Fig. 1 shows that there are
 243 infinitely many solutions to (20) (top panel) and one or two solutions to (21) depending on
 244 α_{\pm} (bottom panel; in both cases we set $\alpha \equiv \alpha_+ = \alpha_-$). An important parameter is the ratio
 245 of the slopes of the right- and left-hand sides of (20) and (21) at $\lambda = 0$, which in both cases
 246 is

$$\frac{\alpha_+ + \alpha_-}{\kappa^2} \equiv \tilde{\kappa}^{-2}$$

247 When $\tilde{\kappa} < 1$ there is only one solution to (21), and there is a solution of (20) with $\lambda < \pi/2$.
 248 On the other hand, if $\tilde{\kappa} > 1$, there are two solutions to (21) (note that the maximum of the
 249 right-hand side of (21) is 1), and there may or may not be a solution of (20) for $\lambda < \pi/2$.³

250 The solution to (21) gives either a generalization of the barotropic mode, in the case of a
 251 single solution, or two modes that capture the vertical structure of the surface modes. Setting

³Note also that if $\alpha_+ \alpha_- > 4\kappa^2$, the denominator of the right-hand side of (20) goes to 0, but stays finite otherwise: the existence of a 0 in the denominator determines whether there is a solution to (20) with $\lambda < \pi/2$ in the case $\tilde{\kappa}^{-2} > 1$.

$\alpha \equiv \alpha_+ = \alpha_-$, these solutions are plotted as functions of $\tilde{\kappa}$ in Fig. 2: there are two solutions when $\tilde{\kappa} > 1$, but only one otherwise. The limiting solutions discussed in the previous section can be derived explicitly. In the limit $\tilde{\kappa}^2 = \kappa^2/(2\alpha) \ll 1$, the single solution of (21) is given by $\tilde{\lambda} \sim \kappa\sqrt{2/\alpha}$, with eigenfunction $\phi \propto 1$, which can be interpreted as the barotropic mode. For $\tilde{\kappa}^2 \gg 1$, the two solutions can be identified as surface intensified modes, one symmetric and the other antisymmetric about the center of the domain, explicitly given by

$$\phi_0 \propto \cosh\left[\kappa\left(z + \frac{1}{2}\right)\right] \quad \text{and} \quad \phi_1 \propto \sinh\left[\kappa\left(z + \frac{1}{2}\right)\right],$$

with eigenvalues $\mu_0/\alpha = \kappa \tanh \kappa$ and $\mu_1/\alpha = \kappa \coth \kappa$. For $\kappa \gg 1$, the eigenvalues are nearly identical, so that linear combinations of the eigenfunctions will also satisfy the eigenvalue problem — in particular, one can construct separate upper-surface and lower-surface modes. For real λ , the right-hand side of (20) tends to zero for both large and small κ , leading to eigenvalues $\lambda_n = n\pi$, $n = 1, 2, \dots$. The eigenfunctions, however, differ in the two cases: for $\tilde{\kappa} \ll 1$, they have the standard form $\phi_n \propto \cos(n\pi z)$, but for $\tilde{\kappa} \gg 1$, they are $\phi_n \propto \sin(n\pi z)$. The first four modes, for $\alpha = 1$ and a range of κ are plotted in Fig. 3.

b. *An oceanic special case*

Here we consider a case that is potentially the most relevant to the ocean, where shears near the surface may lead to surface-intensified modes, while the quiescent abyss may be more naturally represented by the standard boundary condition, $\phi' = 0$ at the bottom. The relevant limits for this case are $\alpha_+ \ll 1$ and $\alpha_- \rightarrow \infty$, in which case the eigenvalue problem reduces to

$$(s\phi'_n)' = -\lambda_n^2 \phi_n, \quad \text{with} \quad \phi_n|_{z=0} = 0, \quad \phi'_n|_{z=-1} = 0, \quad (22a)$$

$$(s\phi'_0)' - \kappa^2 \phi_0 = 0, \quad \text{with} \quad s\phi'_0|_{z=0} = \frac{\mu_0^2}{\alpha_+} \phi_0, \quad \phi'_0|_{z=-1} = 0. \quad (22b)$$

to leading order in α_+ . The solutions ϕ_n , $n = 1, 2, \dots$ to (22a) describe interior modes, while ϕ_0 is the solution to (22b) with $\mu_0^2/\alpha_+ = O(1)$ and represents a zero PV, surface-intensified mode.

Note that the structure of the interior modes, like that of the standard baroclinic modes, is independent of κ ; the normalization of the mode energy that we have chosen however leads to κ -dependent normalization factors. Since we concentrate on the leading-order approximation to the eigenvalue problem as $\alpha_+ \rightarrow 0$, all the modes, including the surface-intensified one, are independent of α_+ and so are the normalisation factors (because the energy does not involve α_+). Only the eigenvalue μ_0^2 depends (linearly) on α_+ , although the approximation $\mu_0^2 = 0$ can be made to conclude, in particular, that the surface-intensified mode has a generalized enstrophy which vanishes to leading order.

Recently, Scott and Furnival (2012) proposed to use the eigenfunctions of (22a), forming what they term a Dirichet basis, in conjunction with the barotropic mode. While this set of functions, like that obtained by adding a surface mode to the standard baroclinic basis (Lapeyre 2009), does not diagonalize the energy, it is remarkable that this is achieved by the complete set of solutions of (22a) and (22b), that is, by the Dirichlet basis plus a surface mode.

For constant N (or $s = 1$), the solutions to (22) may be computed explicitly; they are

$$\phi_0 = A \cosh[\kappa(z + 1)], \quad A \equiv \sqrt{\frac{2}{\kappa \sinh(2\kappa)}} \quad (23a)$$

$$\phi_n = B \sin \left[\left(n - \frac{1}{2} \right) \pi z \right], \quad B \equiv \sqrt{\frac{2}{\pi^2 (n - 1/2)^2 + \kappa^2}} \quad (23b)$$

with eigenvalues $\mu_0^2 = \alpha_+ \kappa \tanh \kappa$ (corresponding to $\tilde{\lambda} \simeq \kappa - (\alpha_+/2) \tanh \kappa$) and $\lambda_n = (n - 1/2)\pi$ with $n = 1, 2, \dots$. Their dimensional form was given by (2) in the introduction. Again, note that the dependence on κ of the coefficient for the interior modes is due to the normalization choice, but is irrelevant for the projection of data.

4. Use of new basis for the projection of simulated data

As a demonstration, we use the new basis to project the energy in three simulated turbulent flows, each generated by baroclinic instability of a fixed mean state in a horizontally-

periodic quasigeostrophic model. The numerical model is spectral in the horizontal, and finite-difference in the vertical — it is the same as used in, for example, Smith and Ferrari (2009). Energy is dissipated by linear bottom drag, and enstrophy is removed by a highly scale-selective exponential cutoff filter (Smith et al. 2002). In all cases, the model resolution is $512 \times 512 \times 100$.

We analyze results from three simulations. These first two are based on highly idealized flows, and will be used to demonstrate the fundamental structure of the basis, and how the partition of energy depends on both the nature of the flow, and on the choice of the nondimensional weights α_{\pm} . The third simulation is based on a more realistic, ocean-like mean state, and is designed to explore the oceanic special case considered at the end of the last section. To project the simulated data onto the new basis, one must consider the generalized matrix eigenvalue problem that results from the particular vertical discretization used in the model. The details of the construction of the basis in this discretization are given explicitly Appendix B.

a. Idealized ‘interior’ and ‘surface’ baroclinic instability simulations

Both idealized flows have constant stratification $s = 1$, a ratio of domain scale to deformation scale equal to 4 and $\beta = 0$, but mean states that generate different types of baroclinic instability. The first simulation, is forced by an ‘interior instability,’ with a mean flow that projects onto the first (standard) baroclinic mode, $U(z) = \cos \pi z$. Flows of this type are unstable due to a sign change of the mean interior PV gradient, but have no mean SB gradients, since $B_y^{\pm} \propto U_z|_{z=0,-1} = 0$ — we refer to this simulation as BC1. The second flow is forced by an Eady mean state, with a linear mean shear $U(z) = z$, so the instability is driven by mean SB gradients $B_y^{\pm} = 1$, resulting in energy generation near the two surfaces.

The simulations are run to statistically steady state, and snapshots of the steady-state prognostic fields of each are used to compute horizontal (total) energy spectra. The upper panels of Fig. 4, display the horizontal spectra for the BC1 (left) and Eady (middle) simu-

316 lations for a few vertical levels z (the right-hand column plots will be discussed in the next
 317 subsection). It is immediately apparent that the energy in the BC1 simulation is spread
 318 rather evenly over depth; by contrast, the energy in the Eady simulation is largely concen-
 319 trated at the two surfaces. The panels in the middle row of Fig. 4 show the first few modes
 320 of the energy projected onto the standard basis, $\phi_n(z) \propto \cos(n\pi z)$, $n = 1, 2, \dots$ (the baro-
 321 clinic modes) and $\phi_0 \propto 1$ (the barotropic mode). Consistent with the z -dependence of the
 322 energy in the upper panel, the energy in BC1 is largely captured by the barotropic and first
 323 baroclinic modes. By contrast, the energy in the Eady case seems to be distributed evenly
 324 across the barotropic and a large number of baroclinic modes, effectively demonstrating the
 325 failure of the standard modes to provide any insight into the energy partition in a case with
 326 large energy near the surfaces.

327 The bottom panels of Fig. 4 display the energy spectra for the first few modes in the
 328 projection onto the new basis (BC1, left panel; Eady, middle panel). Anticipating that the
 329 BC1 simulation is best represented by the standard baroclinic basis (recovered from the
 330 generalized basis in the limit $\alpha_{\pm} \gg 1$), while the Eady simulation is best represented on the
 331 generalized basis in the limit $\alpha_{\pm} \ll 1$, we chose $\alpha_{\pm} = 10^6$ for the former and $\alpha_{\pm} = 10^{-4}$ for
 332 the latter. As is apparent, the generalized basis with the appropriate weights more efficiently
 333 captures the surface energy in the Eady simulation much better than the standard basis.

334 To quantify the choice of α_{\pm} , we consider the projection of energy in both the BC1
 335 and Eady simulations with the generalized basis using weights ranging from $\alpha_{\pm} = 10^{-3}$ to
 336 10^3 (always holding $\alpha = \alpha_+ = \alpha_-$) and ask, for what weights is the energy captured by
 337 the least number of modes? A simple diagnostic for this, the ratio of the energy contained
 338 in the first two modes to the total energy as a function of α , is shown in in Fig. 5. The
 339 results indicate that extreme values of α are best suited for the BC1 ($\alpha \rightarrow \infty$) and Eady
 340 ($\alpha \rightarrow 0$) simulations, thus confirming our choice for Fig. 4. In the next section we examine
 341 a third simulation where the interior and surface contributions are more balanced, so that
 342 intermediate values of α_{\pm} may be expected to be relevant.

b. *A semi-realistic oceanic simulation*

The third simulation is driven by a mean state typical of the mid-latitude ocean. It uses an exponential mean stratification $N^2 = N_0^2 \exp(z/h)$, so that $s = \exp(-z/h)$, with $h = 0.2$, intended to represent the pycnocline. The mean shear is $U(z) = h(z+1-h) \exp(z/h) + g(z) + C$, where $g(z)$ is the first standard baroclinic eigenfunction of the operator $(sg')' = -\lambda^2 g$, with $g' = 0$ at $z = 0, -1$, so that U is surface-intensified with $U'(0) = 1$ and $U'(-1) = 0$. The constant C is set to ensure $\int_{-1}^0 U(z) dz = 0$. Both $U(z)$ and $N(z)$ are plotted in the top panel of Fig. 6. Note that U is baroclinically unstable due to both an internal sign change of the mean PV gradient, and to the interaction of the mean interior PV gradient Q_y with the mean upper SB gradient B_y^+ . Consistent with the assumptions of the ocean modes, the lower SB gradient $B_y^- = 0$. The ratio of the domain scale to the first baroclinic deformation radius (as determined by λ^{-1}) is 5. The nondimensional Coriolis gradient $\beta U_0 L_D^{-2} = 1.2$, and energy is dissipated by a linear drag $r L_d U_0^{-1} = 0.4$. The steady-state turbulent flow has a complicated vertical structure, as evidenced by the vertical slice of the PV shown in Fig. 7.

The energy spectra for the flow are shown in the right panels of Fig. 4, just as for the BC1 and Eady cases. The energy spectra by vertical level again indicates a very surface-intensified flow, but this time, the flow falls off from a $-5/3$ spectral slope to a more energetic interior than was the case for the Eady simulation. Projection onto the standard vertical modes (middle right panel) indicates a peak in the barotropic mode, but otherwise energy is spread evenly over a large number of baroclinic modes. Projection onto a generalized basis is shown in the bottom right panel. For this simulation with no buoyancy activity at the bottom, it is natural to use a basis with $\alpha_- \rightarrow \infty$. The maximum in the ratio of the energy in modes 1 and 2 to total energy shown in Fig. 5 suggests that the value $\alpha = \alpha_+ = 2$ is appropriate. The first few modes of the corresponding basis are shown in the bottom panels of Fig 6. This is the basis chosen for Fig. 4, and indicates that the projection is very effective, with most of the energy captured by the surface and modified first baroclinic modes. An alternative basis is the ‘oceanic’ basis of section b which takes $\alpha_+ \ll 1$. The spectra obtained with this

basis (not shown) are essentially identical to those obtained for $\alpha_+ = 2$. This suggests that the results are insensitive to the precise value of α_+ and that ‘oceanic’ basis may be a good default choice to analyse typical ocean data.

5. Conclusion

This paper presents a family of basis functions designed for the projection of three-dimensional ocean velocity data. The bases diagonalize both the quasigeostrophic energy and a generalization of the quasigeostrophic potential enstrophy that includes contributions from the buoyancy variances at the upper and lower surfaces. The family of bases is parameterized by the weights α_{\pm} assigned to the surface buoyancy variances — the standard baroclinic modes are recovered in the limit $\alpha_{\pm} \rightarrow \infty$, but the modes obtained in the opposite limit allow for efficient representation of the surface buoyancy variances. The bases should prove advantageous in a number of applications, from projection of observations to the derivation of highly truncated theoretical models. Their main drawback compared to the standard basis of baroclinic modes is the dependence of the modes on the wavenumber κ which implies a lack of separation between the horizontal vertical structure in physical space. This drawback is unavoidable if some of the modes are to reflect the SQG contribution; it is minimised for the ‘oceanic’ basis obtained for $\alpha_+ \rightarrow 0$, $\alpha_- \rightarrow \infty$ since all but one modes have a κ -independent structure.

The limit $\alpha_- \rightarrow \infty$ would seem a natural choice of generalized basis for typical ocean conditions takes because of the relative lack of buoyancy activity at the bottom. Regarding α_+ , an optimal value can in principle be chosen by inspecting the spectra for a range of values or by using a diagnostic such as that of Fig. 5. However, some simpler rules of thumb would be desirable. Intuitively, one might expect that the optimal values of α_{\pm} are those that balance the contributions of the enstrophy Z_{κ} and of the surface-buoyancy variance B_{κ}^+ in the generalized enstrophy $P_{\kappa} = Z_{\kappa} + \alpha_+ B_{\kappa}^+$. Some support for this intuition is provided

by Fig. 8 which shows Z_κ , B_κ and their ratio as a function of κ for the ocean simulation. The figure shows a ratio Z_κ/B_κ^+ that is around 5 for a broad range of κ , roughly consistent with the value $\alpha_+ = 2$ indicated by Fig. 5. There is, however, a peak around $\kappa = 4$ and a substantial increase for $\kappa \gtrsim 20$, which suggest that better results could be obtained by allowing α_+ to depend on κ . We have not explored this intriguing possibility here.

As an alternative to the ratio Z_κ/B_κ^\pm , it would be useful to relate more directly the value of the weights α_\pm most appropriate to project a flow on the large-scale characteristics of the flow. Since for flows driven by instabilities, Z_κ and B_κ^\pm are related to the large-scale PV and surface-buoyancy gradients Q_y and B_y^\pm , it is plausible that the ratio Q_y/B_y^\pm can be used as a guide for the choice of the weights.

The advent of higher-resolution satellite observations, expected when the Surface Water Ocean Topography satellite becomes operational (Fu and Ferrari 2008), will improve our understanding of upper-ocean submesoscale dynamics only to the extent that we can connect surface observations with the three-dimensional structure of the flow below the surface. The basis derived and demonstrated here may prove a useful tool in this goal.

Acknowledgments.

KSS acknowledges the support of both NSF award OCE-0962054 and ONR award N00014-09-01-0633, and helpful conversations with Shane Keating and Xiao Xiao. JV acknowledges the support of a Leverhulme Research Fellowship and the hospitality of the Courant Institute where this research was initiated.

416 Derivation details

Here we prove a few relevant facts about the eigenvectors and eigenvalues of (9). First, we show that the operator \mathcal{E} is self-adjoint, e.g. $\langle \xi_m, \mathcal{E} \xi_n \rangle = \langle \mathcal{E} \xi_m, \xi_n \rangle$. Expanding the left-hand side and integrating by parts, we find

$$\begin{aligned}
 \langle \xi_m, \mathcal{E} \xi_n \rangle &= \frac{1}{H} \int_{z^-}^{z^+} -\bar{\xi}_m \phi_n \, dz + \bar{\xi}_m^+ \phi_n(z^+) - \bar{\xi}_m^- \phi_n(z^-), \\
 &= \frac{1}{H} \int_{z^-}^{z^+} -\phi_n \left(\frac{f^2}{N^2} \bar{\phi}_m' \right)' + \kappa^2 \bar{\phi}_m \phi_n \, dz \\
 &\quad + \frac{f^2}{HN^2(z^+)} \bar{\phi}_m'(z^+) \phi_n(z^+) - \frac{f^2}{HN^2(z^-)} \bar{\phi}_m'(z^-) \phi_n(z^-), \\
 &= \frac{1}{H} \int_{z^-}^{z^+} \frac{f^2}{N^2} \phi_n' \bar{\phi}_m' + \kappa^2 \bar{\phi}_m \phi_n \, dz, \\
 &= \langle \mathcal{E} \xi_m, \xi_n \rangle
 \end{aligned}$$

417 since the expression on the penultimate line is clearly symmetric. The self-adjointness of \mathcal{P}
 418 as well as the positive definiteness is obvious.

419 To establish the completeness of the basis of the eigenvector ξ_n , we rewrite the eigenvalue
 420 problem in the standard form $\mathcal{A} \xi_n = \mu_n^{-2} \xi_n$, where $\mathcal{A} = \mathcal{P}^{-1} \mathcal{E}$ is positive definite and self-
 421 adjoint. This operator is compact when acting on the Hilbert space of vectors \mathbf{Q} with
 422 bounded norm $\langle \mathbf{Q}, \mathbf{Q} \rangle$. This is because it is essentially an integral operator with continuous
 423 kernel — the Green's function of the operator $(s\phi')' - \kappa^2 \phi$ (e.g. Debnath and Mikusiński
 424 1998, section 4.8). The Hilbert-Schmidt theorem (Debnath and Mikusiński 1998, section
 425 4.10) then applies to guarantee that every vector \mathbf{Q} has a unique convergent expansion in
 426 terms of the ξ_n .

Discrete eigenvalue problem and numerical computation of modes

Here we construct the discrete version of the eigenvalue problem. Assuming a constant discrete coordinate z_j on J grid points, with $z_1 = 0$ at the top, $z_J = -H$ at the bottom, and a constant finite difference $\Delta z = z_j - z_{j+1}$, the mean stratification is $N_0^2 = (g/\rho_0)\overline{\Delta\rho}/\Delta z$, where $\overline{\Delta\rho} = \rho_J - \rho_1$ is the average background density jump between levels, $\rho_j = \rho(z_j)$ is the background density, and ρ_0 is the average density. The parameter $s = N_0^2/N^2$ is discretized as $s_j = s(z_{j+1/2}) \equiv \overline{\Delta\rho}/(\rho_{j+1} - \rho_j)$, thus s_j is offset by a half space from ρ_j . In this discretization, the SBs and PV are

$$\begin{aligned} b^+ &= \frac{f^2}{N_0^2 H} s\psi'|_{z=0} \longrightarrow L_D^{-2} \frac{s_1}{\delta} (\psi_1 - \psi_2) \\ b^- &= \frac{f^2}{N_0^2 H} s\psi'|_{z=-1} \longrightarrow L_D^{-2} \frac{s_{J-1}}{\delta} (\psi_{J-1} - \psi_J) \\ q &= \left(\frac{f^2}{N_0^2} s\psi' \right)' - \kappa^2 \psi \longrightarrow L_D^{-2} \frac{1}{\delta^2} [s_{j-1}\psi_{j-1} - (s_{j-1} + s_j)\psi_j + s_j\psi_{j+1}] - \kappa^2 \psi_j, \end{aligned}$$

where $\delta \equiv \Delta z/H$ and $L_D \equiv N_0 H/f$. Nondimensionalizing $\kappa \mapsto [L_D^{-1}] \kappa$, $\psi \mapsto [L_D^2 T^{-1}] \psi$ and $(q, b^\pm) \mapsto [T^{-1}] (q, b^\pm)$ (for some timescale T), the discrete PV/SBs and streamfunction are related as

$$\mathbf{Q} = \mathbf{A}\psi,$$

433 where

$$A = \frac{1}{\delta^2} \begin{pmatrix} \delta s_1 & -\delta s_1 & 0 & \dots & 0 \\ s_1 & -(s_1 + s_2 + \delta^2 \kappa^2) & s_2 & 0 & \dots & 0 \\ & & & \dots & & \\ 0 & \dots & 0 & s_{J-2} & -(s_{J-2} + s_{J-1} + \delta^2 \kappa^2) & s_{J-1} \\ 0 & \dots & 0 & & \delta s_{J-1} & -\delta s_{J-1} \end{pmatrix}. \quad (B1)$$

434 Defining the operators

$$B = \begin{pmatrix} 1 & 0 & \dots & 0 \\ 0 & \delta & \dots & 0 \\ & & & \\ 0 & \dots & \delta & 0 \\ 0 & \dots & 0 & 1 \end{pmatrix} \quad \text{and} \quad F = \begin{pmatrix} 1 & 0 & \dots & 0 \\ 0 & -1 & \dots & 0 \\ & & & \\ 0 & \dots & 0 & -1 \end{pmatrix}, \quad (B2)$$

435 one sees that B plays the part of the inner product, e.g. $\langle \xi_1, \xi_2 \rangle \rightarrow \xi_1^T B \xi_2$ and F accomplishes
436 the awkward sign changes in the definition of the operator \mathcal{E} . The energy in wavenumber κ is

$$E_\kappa = \frac{\delta}{2} \left[\sum_{j=1}^{J-1} s_j \left| \frac{\psi_j - \psi_{j-1}}{\delta} \right|^2 + \kappa^2 \sum_{j=2}^{J-1} |\psi_j|^2 \right] = \frac{1}{2} \psi^* F B A \psi.$$

437 For consistency with the theoretical development in section 2, we may also write the energy
438 in terms of the vector $Q = A\psi$,

$$E_\kappa = \frac{1}{2} Q^* B F A^{-1} Q = \frac{1}{2} Q^* B \mathcal{E} Q$$

439 where the symmetry of F and B were used, and $\mathcal{E} \equiv F A^{-1}$ is defined to make the discrete
440 version of the energy operator defined in (8) perfectly clear.

441 Similarly, the generalized enstrophy in wavenumber κ is

$$P_\kappa = \frac{1}{2} Q^* B \mathcal{P} Q$$

442 where we define

$$\mathcal{P} = \begin{pmatrix} \alpha_+ & 0 & \dots & 0 \\ 0 & 1 & \dots & 0 \\ 0 & \dots & 1 & 0 \\ 0 & \dots & 0 & \alpha_- \end{pmatrix}$$

443 to make clear the analogy with the generalized enstrophy operator defined in (8).

444 Now note that $\mathbf{B}\mathcal{E}$ and $\mathbf{B}\mathcal{P}$ are both symmetric (the former can be verified by checking
445 that $\mathbf{F}\mathbf{B}\mathbf{A}$ is symmetric), so we can simultaneously diagonalize the two quadratic forms E_κ
446 and P_κ by solving the generalized eigenvalue problem $\mathbf{B}\mathcal{P}\boldsymbol{\xi}_j = \mu_j^2 \mathbf{B}\mathcal{E}\boldsymbol{\xi}_j$ or, in matrix form

$$(\mathbf{B}\mathcal{P})\mathbf{X} = (\mathbf{B}\mathcal{E})\mathbf{X}\mathbf{M}^2$$

447 where \mathbf{X} is the matrix with columns $\boldsymbol{\xi}_j$ and \mathbf{M}^2 has μ_j^2 along its diagonal and zeros elsewhere.

448 Solutions to this generalized eigenvalue problem obey the orthogonality relations

$$\mathbf{X}^\top \mathbf{B}\mathcal{E}\mathbf{X} = \mathbf{I} \quad \text{and} \quad \mathbf{X}^\top \mathbf{B}\mathcal{P}\mathbf{X} = \mathbf{M}^2, \quad (\text{B3})$$

449 which are analogous to (12) and (13), respectively.

450 In practice, it is more convenient to define a streamfunction eigenfunction $\boldsymbol{\phi}$ such that
451 $\mathbf{A}\boldsymbol{\phi} = \boldsymbol{\xi}$, so that the generalized eigenvalue problem can be rewritten as $\mathbf{F}\mathcal{P}\mathbf{A}\boldsymbol{\phi}_j = \mu_j^2 \boldsymbol{\phi}_j$, or
452 in matrix form

$$\mathbf{F}\mathcal{P}\mathbf{A}\boldsymbol{\Phi} = \boldsymbol{\Phi}\mathbf{M}^2 \quad (\text{B4})$$

453 where $\boldsymbol{\Phi}$ has $\boldsymbol{\phi}_j$ as its columns. In this case, the orthogonality relations become

$$\boldsymbol{\Phi}^\top \mathbf{F}\mathbf{B}\mathbf{A}\boldsymbol{\Phi} = \mathbf{I} \quad \text{and} \quad \boldsymbol{\Phi}^\top \mathcal{P}\mathbf{B}\mathbf{A}^2\boldsymbol{\Phi} = \mathbf{M}^2, \quad (\text{B5})$$

454 where we've used the fact that $\mathbf{F}^2 = \mathbf{I}$. Finally, writing (B4) as $\boldsymbol{\Phi}^{-1}(\mathbf{A}^{-1}\mathcal{P}^{-1}\mathbf{F})\boldsymbol{\Phi} = \mathbf{M}^2$ and
455 using the first relation in (B5), we have the equivalent of (14),

$$\boldsymbol{\Phi}^{-1}\mathbf{B}\mathcal{P}^{-1}\boldsymbol{\Phi} = \mathbf{M}^{-2} \quad (\text{B6})$$

456 The expansion in the basis of eigenvectors ϕ_n of discrete data is readily expressed in
 457 terms of the matrix Φ . Denoting by ψ the column vector of the streamfunction data (Fourier
 458 transformed in the horizontal) $\psi(z_j)$, the expansion reads

$$\psi = \Phi \mathbf{a}, \tag{B7}$$

459 where $\mathbf{a} = (a_1, \dots, a_J)^\top$ is the column vector of the mode amplitudes. These amplitudes are
 460 obtained from the data using the relation

$$\mathbf{a} = \Phi^\top \mathbf{F} \mathbf{B} \mathbf{A} \psi,$$

461 which is deduced from (B5) and (B7). The total energy at a given wavenumber κ ,

$$E_\kappa = \frac{1}{2} \psi^* \mathbf{F} \mathbf{B} \mathbf{A} \psi = \frac{1}{2} |\mathbf{a}|^2,$$

462 where $*$ denotes the complex (conjugate) transpose, is clearly the sum of the individual
 463 contributions $|a_n|^2/2$ of each mode. Similarly, the generalized enstrophy,

$$P_\kappa = \frac{1}{2} \mathbf{Q}^* \mathbf{B} \mathcal{P} \mathbf{Q} = \frac{1}{2} \psi^* \mathcal{P} \mathbf{B} \mathbf{A}^2 \psi = \frac{1}{2} \mathbf{a}^* \mathbf{M}^2 \mathbf{a},$$

464 is the sum of the contributions $\mu_n^2 |a_n|^2/2$.

REFERENCES

- 467 Blumen, W., 1982: Wave-interactions in quasi-geostrophic uniform potential vorticity flow.
468 *J. Atmos. Sci.*, **39** (11), 2388–2396.
- 469 Bretherton, F. P., 1966: Critical layer instability in baroclinic flows. *Quart. J. Roy. Meteor.*
470 *Soc.*, **92**, 325–334.
- 471 Chelton, D. B., M. G. Schlax, and R. M. Samelson, 2011: Global observations of nonlinear
472 mesoscale eddies. *Prog. in Oceanogr.*, **91**, 167–216.
- 473 Debnath, L. and P. Mikusiński, 1998: *Introduction to Hilbert spaces*. 2d ed., Academic Press,
474 551 pp.
- 475 Fu, L.-L. and R. Ferrari, 2008: Observing oceanic submesoscale processes from space. *EOS*,
476 **89**, 488.
- 477 Goldstein, H., 1980: *Classical Mechanics*. 2d ed., Addison-Wesley.
- 478 Held, I. M., R. T. Pierrehumbert, S. T. Garner, and K. L. Swanson, 1995: Surface quasi-
479 geostrophic dynamics. *J. Fluid. Mech.*, **282**, 1–20.
- 480 Horn, R. A. and C. R. Johnson, 1990: *Matrix Analysis*. Cambridge University Press.
- 481 Isern-Fontanet, J., B. Chapron, G. Lapeyre, and P. Klein, 2006: Potential use of microwave
482 sea surface temperatures for the estimation of ocean currents. *Geophysical Research Let-*
483 *ters*, **33** (24), doi:ARTNL24608.
- 484 Klein, P., B. L. Hua, G. Lapeyre, X. Capet, S. L. Gentil, and H. Sasaki, 2008: Upper ocean
485 turbulence from high resolution 3d simulations. *J. Phys. Oceanogr.*, **38**, 1748–1763.

486 LaCasce, J. H. and A. Mahadevan, 2006: Estimating subsurface horizontal and vertical
487 velocities from sea surface temperature. *J. Marine Res.*, **64**, 695–721.

488 Lapeyre, G., 2009: What mesoscale signal does the altimeter reflect? on the decomposition
489 in baroclinic modes and a surface-trapped mode. *J. Phys. Oceanogr.*, **39**, 2857–2874.

490 Lapeyre, G. and P. Klein, 2006: Dynamics of the upper oceanic layers in terms of surface
491 quasigeostrophy theory. *J. Phys. Oceanogr.*, **36**, 165–176.

492 Le Traon, P. Y., P. Klein, and B. L. Hua, 2008: Do altimeter wavenumber spectra agree
493 with the interior or surface quasigeostrophic theory? *J. Phys. Oceanogr.*, **38**, 1137–1142.

494 Scott, R. B. and D. G. Furnival, 2012: Assessment of traditional and new eigenfunction bases
495 applied to extrapolation of surface geostrophic current time series to below the surface in
496 an idealized primitive equation simulation. *J. Phys. Oceanogr.*, **42**, 165–178.

497 Smith, K. S., G. Boccaletti, C. C. Henning, I. N. Marinov, C. Y. Tam, I. M. Held, and G. K.
498 Vallis, 2002: Turbulent diffusion in the geostrophic inverse cascade. *J. Fluid Mech.*, **469**,
499 13–48.

500 Smith, K. S. and R. Ferrari, 2009: The production and dissipation of compensated thermo-
501 haline variance by mesoscale stirring. *J. Phys. Oceanogr.*, **39**, 2477–2501.

502 Stammer, D., 1997: Global characteristics of ocean variability estimated from regional
503 TOPEX/Poseidon altimeter measurements. *J. Phys. Oceanogr.*, **27**, 1743–1769.

504 Tulloch, R. T. and K. S. Smith, 2009: Quasigeostrophic turbulence with explicit surface
505 dynamics: Application to the atmospheric energy spectrum. *J. Atmos. Sci.*, **66**, 450–467.

506 Wunsch, C., 1997: The vertical partition of oceanic horizontal kinetic energy. *J. Phys.*
507 *Oceanogr.*, **27**, 1770–1794.

List of Figures

- 1 Graphical solutions for eigenvalues with constant N for $\kappa = 1$. The left panel shows the left and right hand sides of Eq. (20), and the right panel shows Eq. (21). 29
- 2 Solutions to (21), with κ scaled by $\sqrt{2\alpha}$, the cutoff separating cases with one or two solutions for imaginary λ . 30
- 3 The first four eigenfunctions ϕ_n for the constant- N case, with $\alpha_+ = \alpha_- = 100$ and $\kappa = 1, 30, 100$. 31
- 4 Energy spectra for the BC1 (left), Eady (middle) and Ocean (right) simulations. Top panels: spectra for selected vertical levels (see legend). Middle: spectra from fields projected onto standard vertical modes (modes 1, 2 and 3–10 are shown). Bottom: spectra from fields projected onto new modes, with $\alpha_+ = \alpha_- = 10^6$ for the BC1 case, $\alpha_+ = \alpha_- = 10^{-4}$ for the Eady case and $\alpha_+ = 2, \alpha_- = 10^6$ for the Ocean case. 32
- 5 Ratio of the energy content of the first two modes to the total energy as a function of $\alpha = \alpha_+ = \alpha_-$ for the BC1 and Eady simulations, and as a function of $\alpha = \alpha^+$ (with $\alpha_- \rightarrow \infty$) for the Ocean simulation. 33
- 6 Left: $N^2(z)$ and $U(z)$ for the Ocean simulation. Middle: the surface mode $\phi_0(z)$ with $\alpha_- \rightarrow \infty$ and $\alpha_+ \ll 1$ (solid) and $\alpha_+ = 2$ (dashed), for a range of wavenumbers κ (see legend). The $\kappa = .1$ lines are on top of each other. Right: The first three interior modes with $\alpha_+ \ll 1$ and $\alpha_- \rightarrow \infty$. 34
- 7 Vertical slice of PV snapshot from the Ocean simulation. The flow has a complicated structure in the upper ocean, masking a more uniform flow at depth. 35

8 Enstrophy Z_κ and surface buoyancy variance B_κ^+ as functions of wavenumber
 κ for the Ocean simulation (lines with slopes -1 and -5/3 are included for
reference). The ratio Z_κ/B_κ^+ , also shown, can be used to guide the choice of
the weight α_+ for an effective projection basis. 36

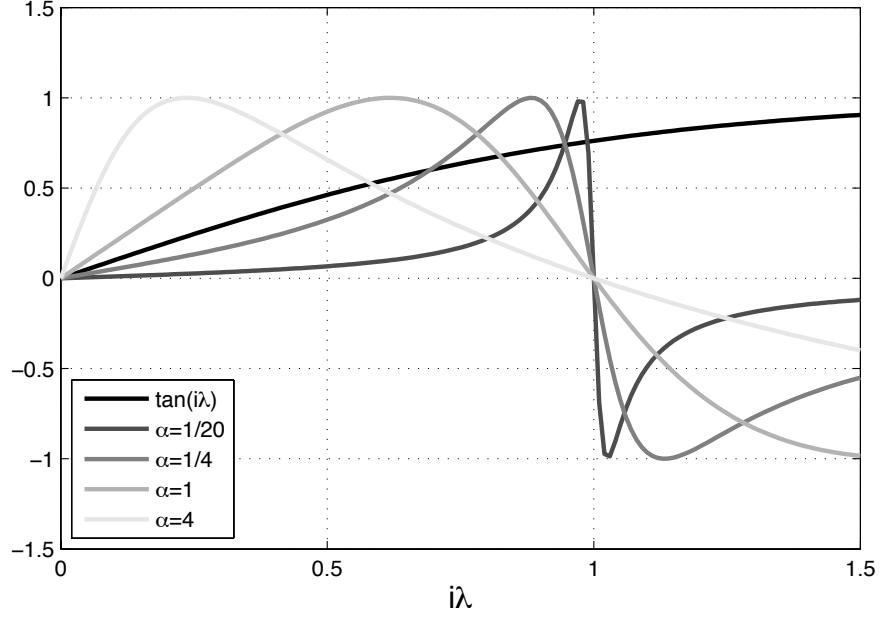
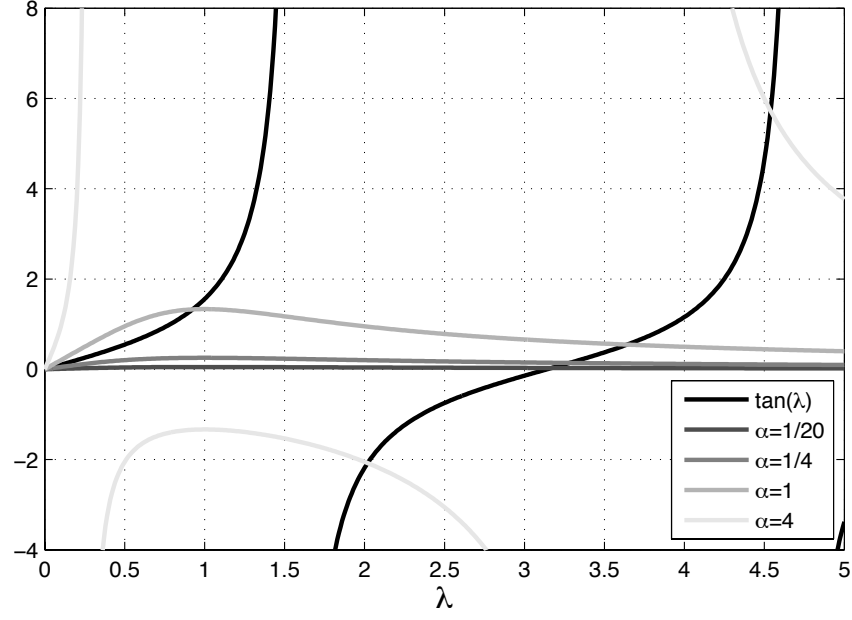


FIG. 1. Graphical solutions for eigenvalues with constant N for $\kappa = 1$. The left panel shows the left and right hand sides of Eq. (20), and the right panel shows Eq. (21).

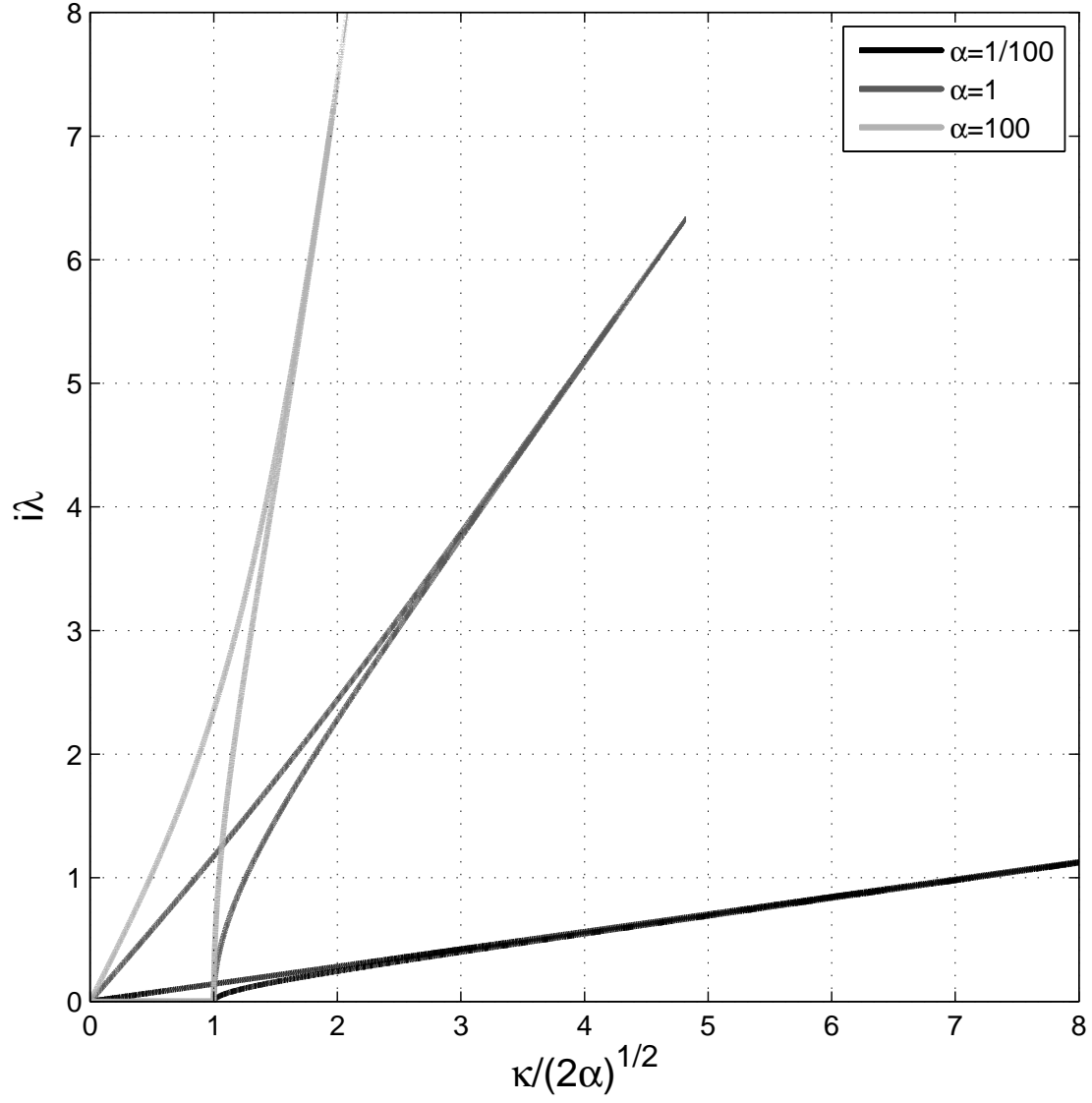


FIG. 2. Solutions to (21), with κ scaled by $\sqrt{2\alpha}$, the cutoff separating cases with one or two solutions for imaginary λ .

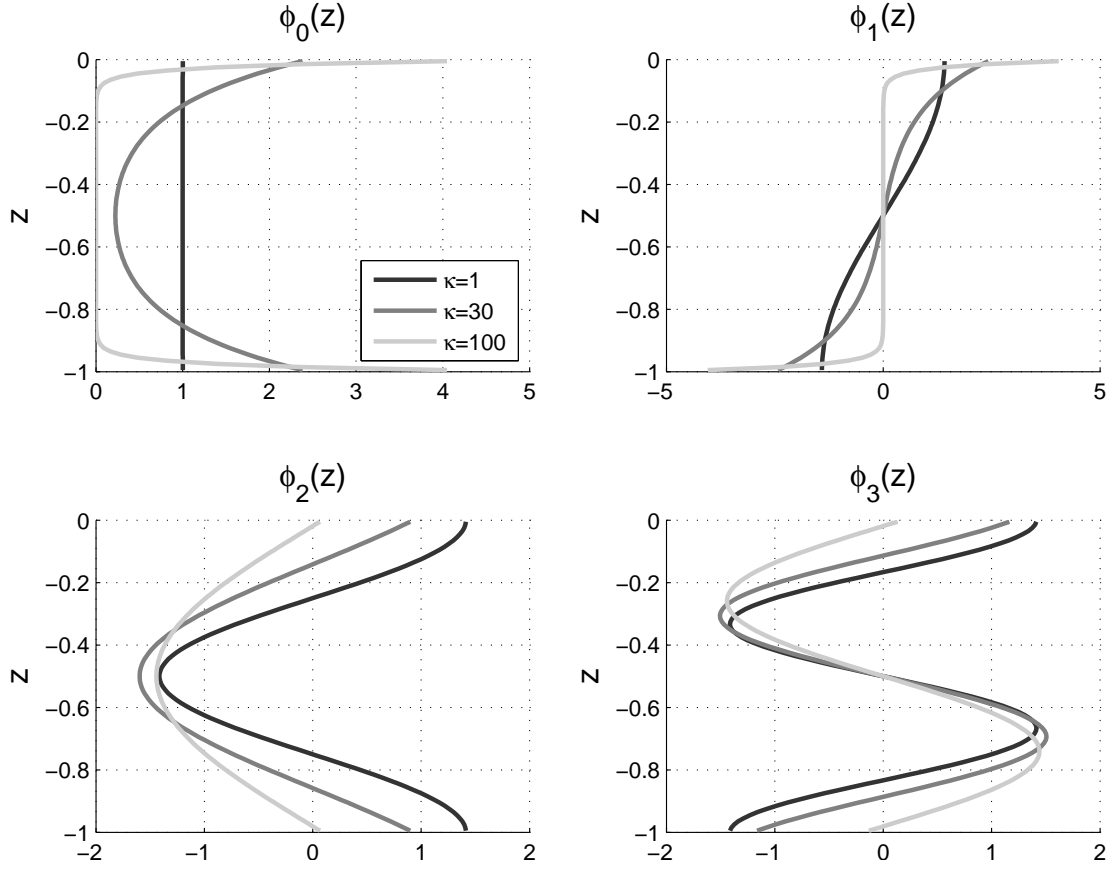


FIG. 3. The first four eigenfunctions ϕ_n for the constant- N case, with $\alpha_+ = \alpha_- = 100$ and $\kappa = 1, 30, 100$.

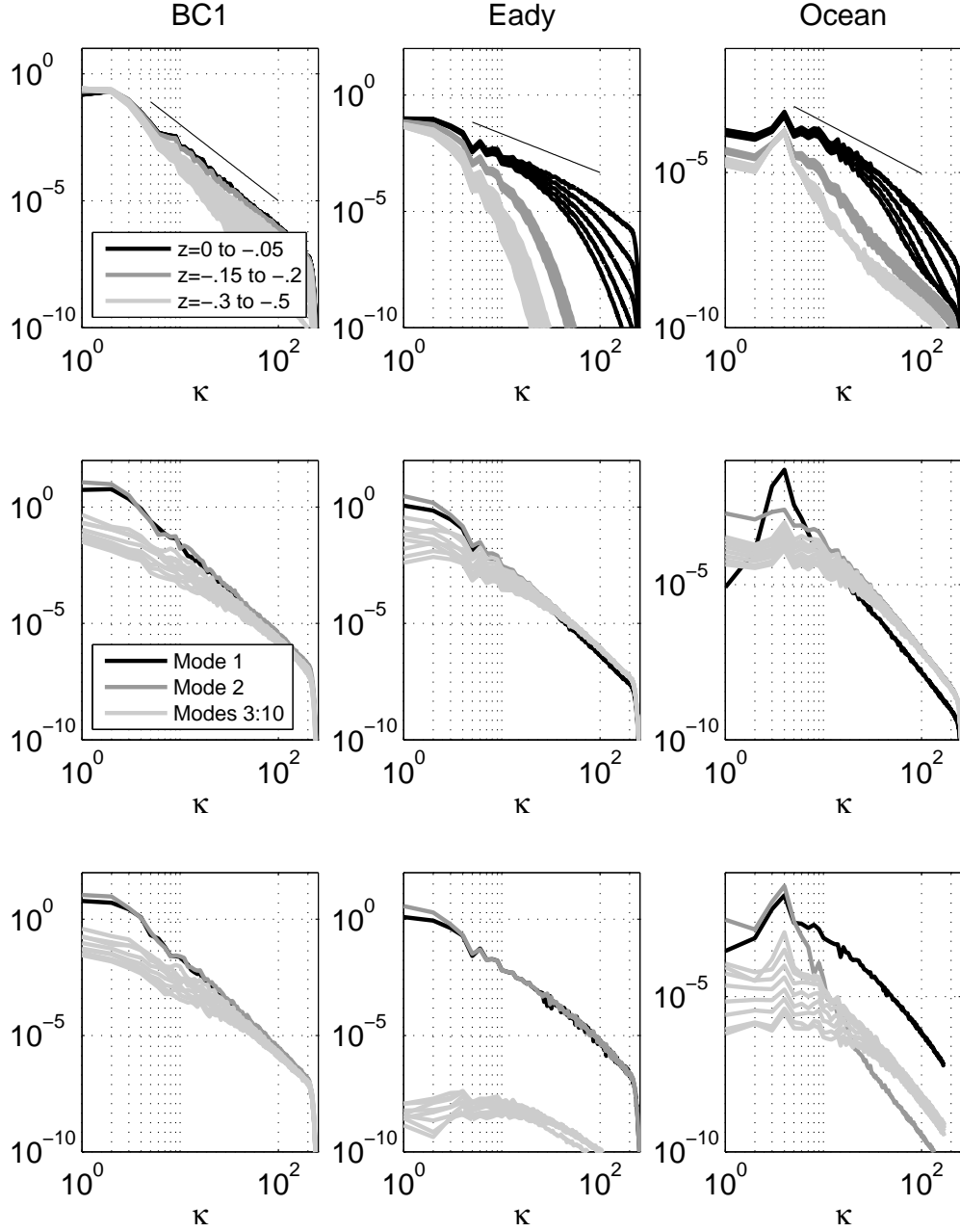


FIG. 4. Energy spectra for the BC1 (left), Eady (middle) and Ocean (right) simulations. Top panels: spectra for selected vertical levels (see legend). Middle: spectra from fields projected onto standard vertical modes (modes 1, 2 and 3–10 are shown). Bottom: spectra from fields projected onto new modes, with $\alpha_+ = \alpha_- = 10^6$ for the BC1 case, $\alpha_+ = \alpha_- = 10^{-4}$ for the Eady case and $\alpha_+ = 2$, $\alpha_- = 10^6$ for the Ocean case.

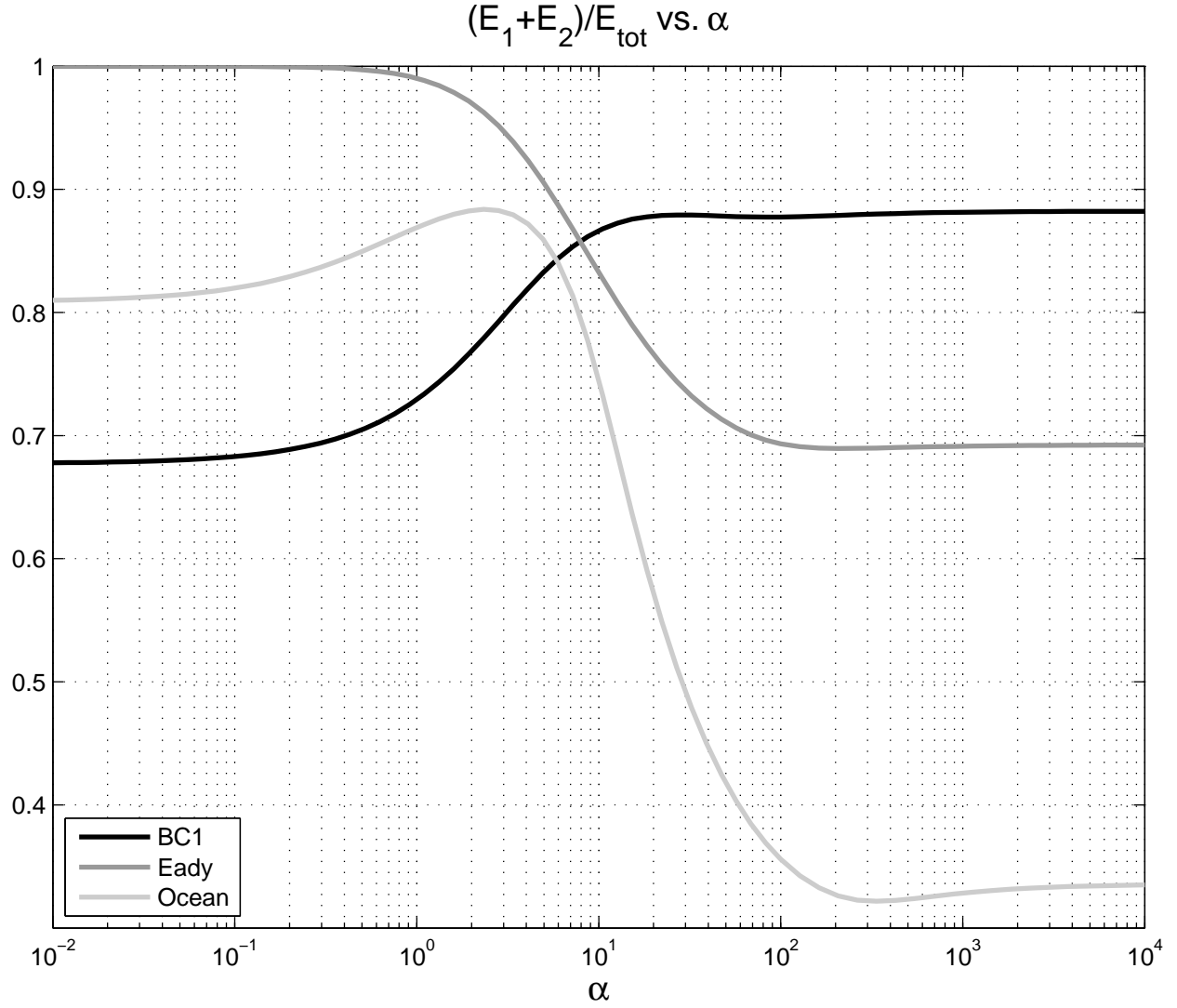


FIG. 5. Ratio of the energy content of the first two modes to the total energy as a function of $\alpha = \alpha_+ = \alpha_-$ for the BC1 and Eady simulations, and as a function of $\alpha = \alpha^+$ (with $\alpha_- \rightarrow \infty$) for the Ocean simulation.

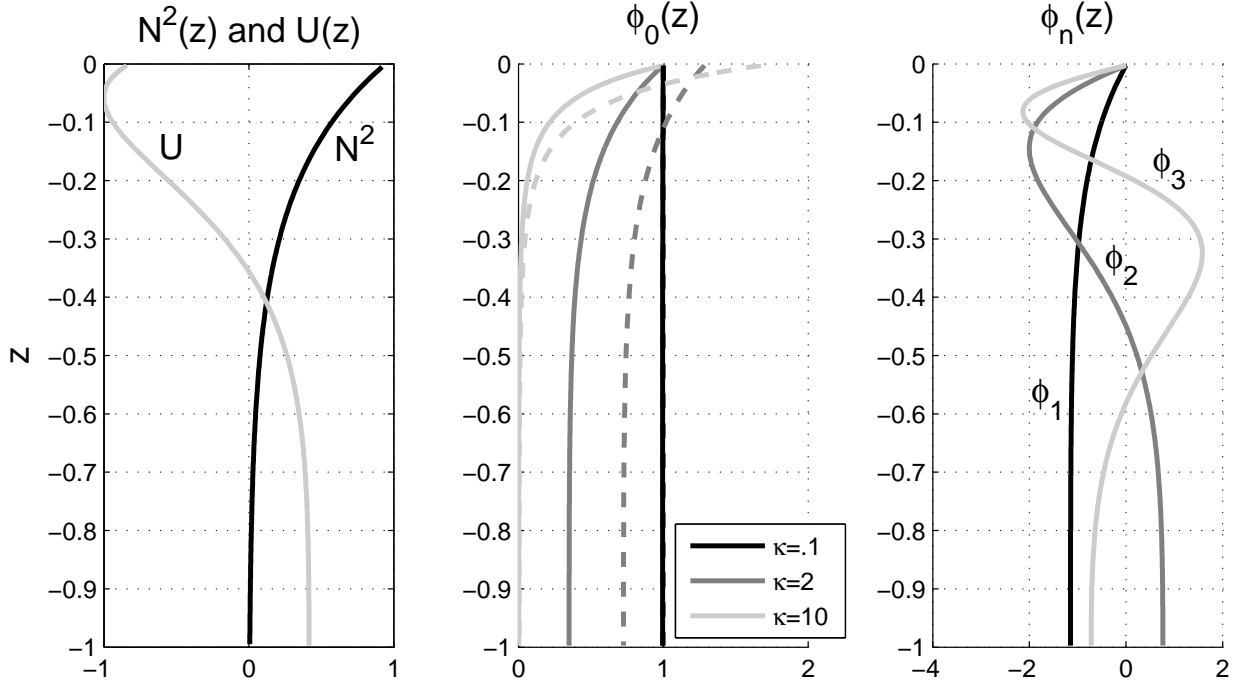


FIG. 6. Left: $N^2(z)$ and $U(z)$ for the Ocean simulation. Middle: the surface mode $\phi_0(z)$ with $\alpha_- \rightarrow \infty$ and $\alpha_+ \ll 1$ (solid) and $\alpha_+ = 2$ (dashed), for a range of wavenumbers κ (see legend). The $\kappa = .1$ lines are on top of each other. Right: The first three interior modes with $\alpha_+ \ll 1$ and $\alpha_- \rightarrow \infty$.

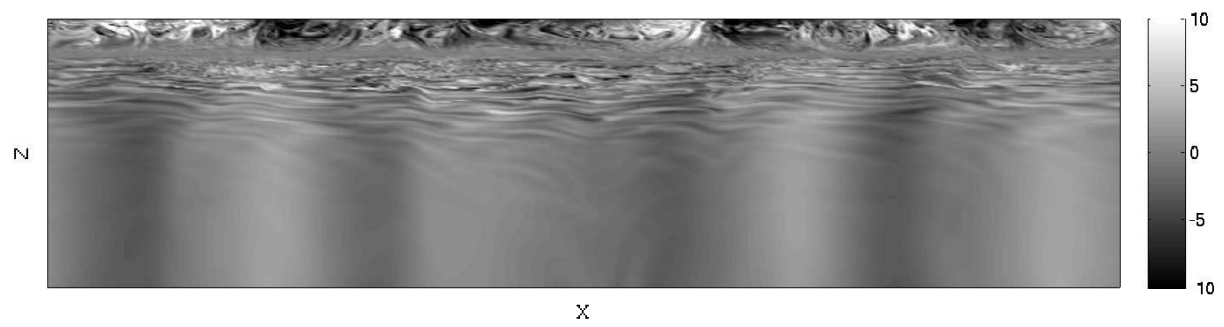


FIG. 7. Vertical slice of PV snapshot from the Ocean simulation. The flow has a complicated structure in the upper ocean, masking a more uniform flow at depth.

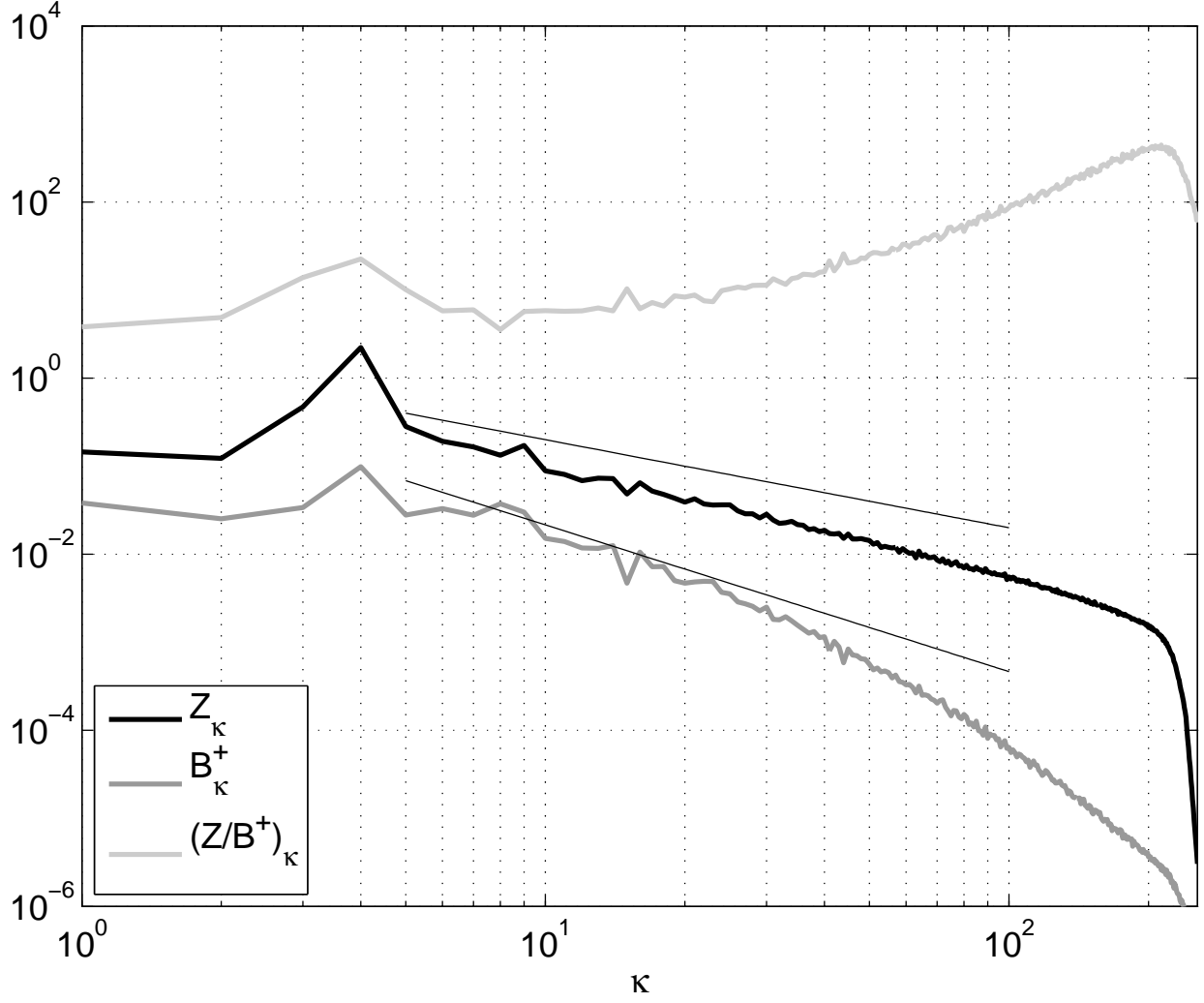


FIG. 8. Enstrophy Z_κ and surface buoyancy variance B_κ^+ as functions of wavenumber κ for the Ocean simulation (lines with slopes -1 and -5/3 are included for reference). The ratio Z_κ/B_κ^+ , also shown, can be used to guide the choice of the weight α_+ for an effective projection basis.